Ultrahigh-Frequency Heterodyne Lock-In Carrierography for Large-Scale Quantitative Multi-Parameter Imaging of Colloidal Quantum Dot Solar Cells

Lilei Hu, Andreas Mandelis, and Qiming Sun

Abstract—**Ultrahigh-frequency heterodyne lock-in carrierography (UHF-HeLIC) is a new near-IR dynamic photoluminescence (PL) camera-based large-area imaging technique. It is specifically developed for investigating dynamic optoelectronic events that occur at very fast diffusion-wave rates ($> = 10$ kHz), above which conventional camera imaging cannot be achieved. The nonlinear combination of two-frequency-modulated photogenerated carrier density waves (CDWs) with a 10 Hz beat frequency was used to generate HeLIC images in the UHF range (up to 270 kHz) above the effective CDW recombination rate. Using sequences of these high-frequency images and UHF-HeLIC theory, carrier lifetime, diffusivity, and diffusion and drift length images were reconstructed from colloidal quantum dot solar cells and used for studying the influence of surface and interface trap states on photocarrier transport processes. The new non-destructive UHF-HeLIC imaging methodology shows excellent potential for industrial inline photovoltaic device characterization, fundamental optoelectronic physical process studies, and various other photoelectronic applications.**

Index Terms—**Carrier lifetime, large-scale imaging, lock-in carrierography, quantum dot, solar cell.**

I. INTRODUCTION

CAMERA-BASED fluorescence imaging has been widely used for inspecting photovoltaic (PV) and optoelectronic materials and devices [1], [2] and in medical science, such as cancer detection, drug delivery tracking, and targeted treatment *in vivo* [3], [4]. However, many optoelectronic events of interest occur at very fast rates (with time constants of micro- and nano-seconds), the properties of which cannot be studied even by the fastest state-of-the-art cameras due to the low frame
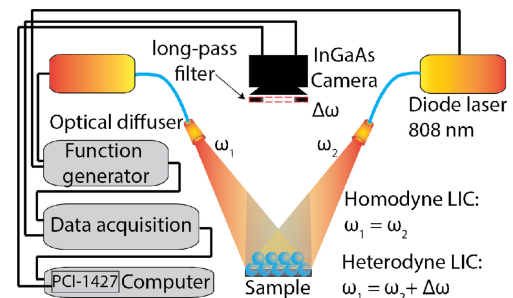
Fig. 1. Experimental setup for homodyne (HoLIC) and ultrahigh-frequency heterodyne (UHF-HeLIC) lock-in carrierography imaging. Two photoexcitation lasers are modulated at the same frequency for HoLIC; instead, they are modulated at two frequency ω_1 and ω_2 with a beat frequency difference of $\Delta\omega$ for HeLIC.

rate and requirements for high exposure time [5], [6]. Nevertheless, large-area PV characterization requires camera based, fast, nondestructive, and contactless imaging methodologies for the study of fundamental carrier transport dynamics and for device quality evaluation to increase solar cell efficiency. Spatially resolved PL and electroluminescence (EL) have been found to be powerful techniques for characterizing silicon wafers [7]–[9] and solar cells [9]–[11]. Unfortunately, steady (DC) PL and EL cannot detect optoelectronic kinetics of surface- and near-subsurface (junction) regions, defects, and electrical parameters of p-n junctions [11], [12]. Additionally, PL and EL cannot monitor electronic transport kinetics and recombination dynamics [13], [14], which are key determining processes for PV energy conversion and dissipation. On the other hand, lock-in amplifier based techniques under frequency-modulated laser excitation can perform dynamic characterization but are limited to a low-frequency range due to camera low frame rates and short exposure times [15]–[17]. Consequently, these techniques cannot resolve fast photocarrier transport processes.

II. INSTRUMENTATION OF HETERODYNE LOCK-IN CARRIEROGRAPHY (HELIC)

To extract high-frequency information from photonic (radiative) emissions from laser-illuminated PV solar cells, we introduced an ultra-high frequency (UHF) HeLIC method. As shown in Fig. 1, two 808-nm diode lasers with a combined

power of 1 sun (0.5 sun each) were modulated at two different frequencies with a beat frequency of 10 Hz. Two optical diffusers were used to obtain evenly distributed laser intensity across the sample surface with small intensity variations (5%). A two-channel function generator was used for frequency modulation and it was connected to a data acquisition card that received image data from the NIR InGaAs camera (Goodrich SU320 KTSW-1.7RT/RS170) and communicated with a frame grabber (NI PCI-1427). The implemented high-speed camera has 320×256 active pixel elements, a bandwidth of 0.9–1.7 μm, 120 fps frame rate, and adjustable exposure times ranging from 0.13 to 16.6 ms. Furthermore, to eliminate the influence of the excitation laser beam, a long-pass filter (Spectrogon LP-1000) was mounted in front of the InGaAs camera, setting the active homodyne (HoLIC) and UHF-HeLIC bandwidth between 1.0–1.7 μm, which corresponds to the near bandedge and shallow trap-state or doping-associated radiative recombination for our colloidal quantum dot (CQD) solar cells. HeLIC imaging frequency range has been defined as UHF when $f_{UHF} > 1/f$ where f is the effective lifetime of the contrast-generating carrier density wave (CDW). Only in this frequency range it is possible to generate quantitative imaging of the transport processes controlling the PV photonic-to-electronic energy conversion process. This is the reason for which carrier lifetimes in the ms to sub-μs range and other transport properties have not been imaged quantitatively over an entire solar cell before the present introduction of UHF-HeLIC and its application to CQD solar cells. The purpose of signal heterodyning is to generate a low frequency beat under high-frequency laser pumping, as the camera is only capable of capturing images at low frequencies, which, however, contain high frequency information. In this manner, lock-in carrierography UHF imaging as defined previously can be achieved. This is unlike conventional single-detector-based non-imaging UHF measurements in fields of electronics where physical electronic processes occur other than radiative recombination and can be captured by ultrafast single-element photodetectors.

III. SIGNAL GENERATION PRINCIPLES AND NONLINEAR RESPONSE OF HeLIC

Given the fact that the photoexcited exciton population has a linear dependence on the incident photoexcitation intensity in a CQD solar cell, as shown in Fig. S1 in the supplementary information, to generate UHF-HeLIC imaging the photoexcitation laser beams were modulated at two ultrahigh angular frequencies (ω_1, ω_2) with a small frequency difference $\Delta\omega$ (i.e., the beat frequency), such that ω_1, $\omega_2 \gg \Delta\omega$, which led to the generation of two CDWs modulated at the corresponding frequencies. These two CDWs can be mixed in a nonlinear signal processing device, a mixer, such as a diode or a transistor [18]. As shown in Fig. S1 in the supplementary information, besides non-radiative decay, the mixer creates a spectrum of CDW frequency responses including those modulated at the difference frequency $\Delta\omega$. In HeLIC solar cell imaging, the sample itself acts as a mixer [19]. The radiative recombination physics of CDW [photocarrier radiometry (PCR)] has been developed by Mandelis et al. [20] as a depth integral of excess free CDW
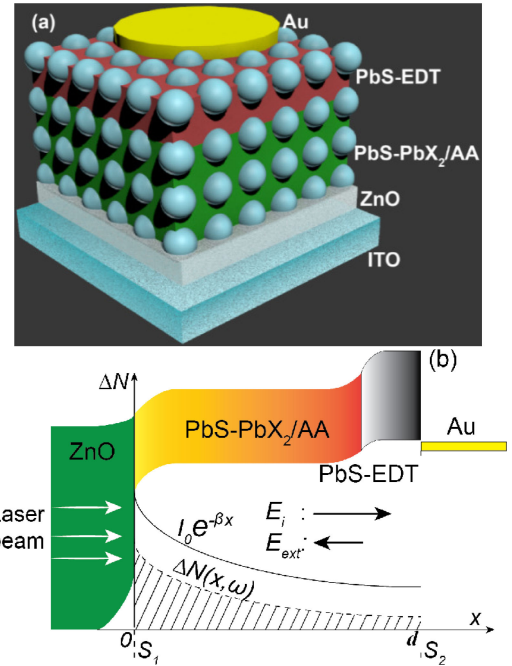

Fig. 2. (a) Schematic of the sandwich structure of the as-fabricated CQD solar cells, and (b) the corresponding energy level structure. PbS-EDT and PbS-PbX$_2$/AA represent EDT (1, 2-ethanedithiol) and PbX$_2$/AA (PbX$_2$: lead halide, AA: ammonium acetate) surface passivated PbS CQDs. The photogenerated carrier-density-wave $\Delta N(x, \omega)$, as well as the intrinsic E_i and external E_{ext} electric fields, are shown. The terms I_0, β, $S_{1/2}$ are incident photon intensity, absorption coefficient, and surface recombination velocity at the front and back interfaces, respectively.

density. Therefore, the signal expression for the detection of radiative PL emissions from PV samples can be described by

$$S(\omega) = F \int_0^d \Delta N(x, \omega) dx \quad (1)$$

where F is an instrumentation coefficient depending on the spectral bandwidth of the *IR* detector and camera, and d is the active layer thickness. $\Delta N(x, \omega)$ is the excess carrier density wave. In UHF-HeLIC, as the laser excitation is modulated at two frequencies with an angular frequency difference $\Delta\omega$, the excess photocarrier wave can be expressed as

$$\Delta N(x, \omega) = 2n_0(x) + A(x, \omega_1)\cos[\omega_1 t + \varphi(x, \omega_1)]$$
$$+ A(x, \omega_2)\cos[\omega_2 t + \varphi(x, \omega_2)] \quad (2)$$

where $n_0(x)$ is the dc component of the modulated excess CDW, $A(x, \omega_j)$ is the amplitude of the cosinusoidally modulated CDW at ω_j ($j = 1, 2$) and φ is the CDW phase. Equations (1) and (2) are only approximate, since PL emission response to photoexcitation intensity is a fundamentally non-linear process with a non-linearity coefficient γ that was generally measured to be between 0.5 and 2, and can be determined by plotting l versus I_0^γ where l represents the PL emission intensity and I_0 stands for the excitation laser power intensity. Hu et al. [19] measured γ of CQD thin films to be in a range between 0.66 and 0.94 depending on different CQD types and testing temperatures. As for the CQD solar cells with a sandwich structure shown in Fig. 2(a) and (b) (details of the sample are provided in the supplementary information, Materials and experimental

system), the nonlinear coefficient γ can be obtained, as shown in Fig. S2(a) in the supplementary information, through fitting the experimental dc image signal versus laser photoexcitation intensity to $I \propto I_0^\gamma$. A nonlinear coefficient γ of 0.60 was extracted, consistent with the requirement for a non-linear process, $\gamma \neq 1$, to generate a HeLIC signal [19], [21]. The excitation-induced light absorption, excess carrier generation and diffusion, and intrinsic and external electric fields are presented in Fig. 2(b) for the derivation of the excess carrier density and the demodulated UHF-HeLIC signal expression for CQD solar cells, as detailed in the supplementary information.

Inserting $\Delta N(x, \omega)$ in (2) into (1) and considering the fully nonlinear response, with the integrand expanded using the binomial theorem in the form

$$\{2n_0(x) + A(x, \omega_1)\cos[\omega_1 t + \varphi_1(x, \omega_1)] + A(x, \omega_2)$$

$$\times \cos[\omega_2 t + \varphi_2(x, \omega_2)]\}^\gamma$$

$$= \sum_{k=0}^{+\infty} \binom{\gamma}{k} \sum_{m=0}^{+\infty} \binom{\gamma - k}{m} [2n_0(x)]^{\gamma-k-m}\{A(x, \omega_1)$$

$$\times \cos[\omega_1 t + \varphi_1(x, \omega_1)]\}^m$$

$$\{A(x, \omega_2)\cos[\omega_2 t + \varphi_2(x, \omega_2)]\}^k \quad (3)$$

and expanding (3) using $\cos^k(\omega t) = 2^{-k} \sum_{m=0}^\infty \binom{k}{m} e^{i(k-2m)\omega t}$, it can be shown that the demodulated HeLIC signal can be finally written as

$$S(\Delta\omega) = F \sum_{m=0}^{+\infty} \sum_{n=0}^{+\infty} \frac{\prod_{i=0}^{2m+2n+1}(\gamma - l)}{4^{m+n} m!(m+1)!n!(n+1)!} \bullet$$

$$\int_0^d \frac{1}{2} n_0(x)^\gamma \left[\frac{A(x, \omega_1)}{n_0(x)}\right]^{2m+1} \left[\frac{A(x, \omega_2)}{n_0(x)}\right]^{2n+1} e^{i\Delta\varphi(x)} dx \quad (4)$$

as only signals modulated at the beat frequency $\Delta\omega = |\omega_2 - \omega_1|$ contribute to UHF-HeLIC. It should be noted that it is difficult to experimentally measure the small HeLIC phase value $\Delta\varphi(x) = |\varphi(x, \omega_2) - \varphi(x, \omega_1)|$ on the order of 10^{-3} degree due to the small beat frequency $\Delta\omega$ in the UHF heterodyne mode ($\omega_1, \omega_2 \gg \Delta\omega$). For CQD-based thin films, $\Delta N(x, \omega)$ has been derived in [22]. In Fig. S2(b) in the supplementary information, the dependence of wideband (1–270 kHz) UHF-HeLIC images on the laser photoexcitation power was investigated using a fixed 1-sun average intensity of modulated spread excitation beam while changing the dc excitation intensity, i.e., $n_0(x)$ in (4) changed proportionally with the excitation intensity that varied from 0.2 to 1.1 sun. It was found that the average amplitude of UHF-HeLIC images decreases with increasing dc photoexcitation intensity, which contrasts with its dc counterpart, as shown in Fig. S2(a) in the supplementary information. The decrease of the UHF-HeLIC signal with dc excitation agrees with (4) due to the decreasing overall dependence on $n_0(x): n_0(x)^{\gamma-2(m+n+1)}; \gamma = 0.6, m, n \geq 0$. Physically, for CQD systems featured with discrete energy bands induced by spatial and energy disorder, the photogenerated excitons cannot dissociate immediately into free charge carriers, in
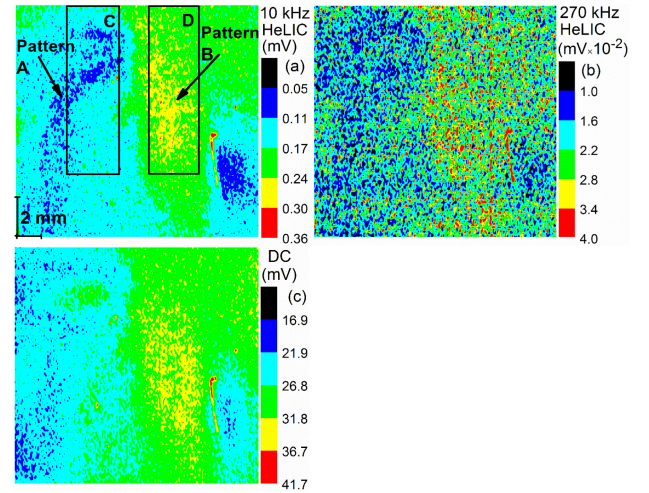

Fig. 3. HeLIC images of a CQD solar cell at various modulation frequencies (a) 1 kHz and (b) 270 kHz. (c) Conventional dc PL image of the same solar cell region was also obtained.

contrast to those generated in continuous energy band semiconductors, such as Si. Therefore, without the assistance of external forces including interdot coupling and material interface effects, excitons are the dominant energy carriers in CQD systems and act as the main radiative recombination sources [19]. This picture is consistent with the HeLIC signal decrease with increasing dc irradiation intensity as the result of increased densities of excitonic traps rendered unoccupied because of optical excitation, leading to increased trapping and decreased exciton dissociation probabilities, followed by decreased radiative recombination. Based on the foregoing dominance of exciton dynamics, Hu *et al.* [19] reported that the coefficient $\gamma = 1$ for excitonic transitions, whereas $\gamma = 0.5$ for carrier recombinations induced by trap- or doping-associated states. Hence, the physical meaning of (4) can be interpreted as an evolution of the well-known exponential relation between photoexcitation and PL, $I \propto I_0^\gamma$, in the framework of UHF-HeLIC. In summary, the expectation of the decreased HeLIC signal with increased dc photoexcitation intensity in (4) and Fig. S2(b) in the supplementary information results from three physical facts: unoccupied trap-state density increases through enhanced photon-absorption-mediated carrier ejection, increased exciton-density-mediated carrier trapping, and the nonlinear nature of radiative PL signal collection in a heterodyne mode.

IV. ULTRA-HIGH FREQUENCY IMAGING

The depth-selective/resolved high-frequency HeLIC image of CQD solar cells (with a structure shown in Fig. 2(a) but without Au electrode deposition) was obtained, as shown in Fig. 3(a). The HeLIC image obtained at 270 kHz is also presented in Fig. 3(b), the highest modulation frequency attained for PL-based PV imaging to-date. It was found that with the increasing modulation frequency (10 to 270 kHz) of the UHF-HeLIC images, the low amplitude pattern A shrinks, whereas the high amplitude pattern B spreads out. With further quantitative investigation, the image contrast is controlled by the modu-

lation frequency-dependent ac diffusion length $L(\omega)$ through $L(\omega) = \sqrt{\frac{D_e \tau}{1 + i\omega\tau}}$ (where D_e is the diffusivity), which enables HeLIC to act as a depth-resolved technique, showing excellent potential for depth-dependent characterization of PV solar cells. UHF-HeLIC images at various modulation frequencies can exhibit different image contrast emerging from electronic property variations with depth. A conventional PL image at dc photoexcitation is presented in Fig. 3(c) for comparison with the UHF-HeLIC images. It is obvious that the UHF-HeLIC images share some similarities with the dc PL image, while adding extra dynamic contrast from the modulation frequency dependence, enabling the study of fast rate carrier transport with cameras. Due to the much lower UHF-HeLIC amplitudes at 270 kHz and the much higher dc PL values when compared with the other UHF-HeLIC images including Fig. 3(a), it should be noted that the color scales of the images in Fig. 3 are not the same. Furthermore, the measurement time is determined by the camera exposure time (usually, several ms) and the measured frequency points (∼30 frequencies). Each measurement conducted in this manuscript lasted less than 1 min. Additionally, the measurement area can be operator adjusted using a diffuser, as long as the excitation power density of the laser is high enough to produce measurable signal-to-noise ratios.

V. CARRIER TRANSPORT PARAMETER IMAGE RECONSTRUCTION

The decrease of HeLIC amplitude with frequency originates in the competition between carrier lifetime-controlled recombination rate and laser modulation frequency initiated generation rate. Physical optoelectronic mechanisms of carrier generation, hopping transport and recombination under frequency-modulated excitation for CQD solar cells, and theoretical signal descriptions responsible for image formation have been developed in the supplementary information and the expression for the demodulated UHF-HeLIC signal is given by

$$S_{he}(\Delta\omega) \propto B(\omega_1)^* B(\omega_2) S_{he}(\omega_1, \omega_2); \omega_1, \omega_2$$
$$\gg \Delta\omega(\text{UHF range}) \quad (5)$$

where $B(\omega_j), j = 1, 2$ is defined as (S13a) in the supplementary information, and $*$ denotes the complex conjugation. The expression for $S_{he}(\omega_1, \omega_2)$ as a function of modulation frequency is given as Eq. (S15). Based on the UHF-HeLIC theory, the carrier lifetimes in CQD solar cells with and without 15-s plasma etching could be obtained. Furthermore, the average lifetimes in regions C and D shown inside the rectangle-circumscribed areas in Fig. 3(a), were best fitted to (5) from the averaged HeLIC pixel amplitudes in each region at each UHF frequency ranging from 1 to 270 kHz. As shown in Fig. 4(a), the frequency-dependent HeLIC amplitudes and their best fits yielded average lifetime measurements for regions C and D equal to 0.56 and 0.63 μs, respectively. The slightly higher value in region D is in agreement with the HeLIC lifetime image, as shown in Fig. 4(b), for the same CQD solar cell obtained through best fitting of a sequence of 27 HeLIC images to (5), each at a different frequency, including those shown in
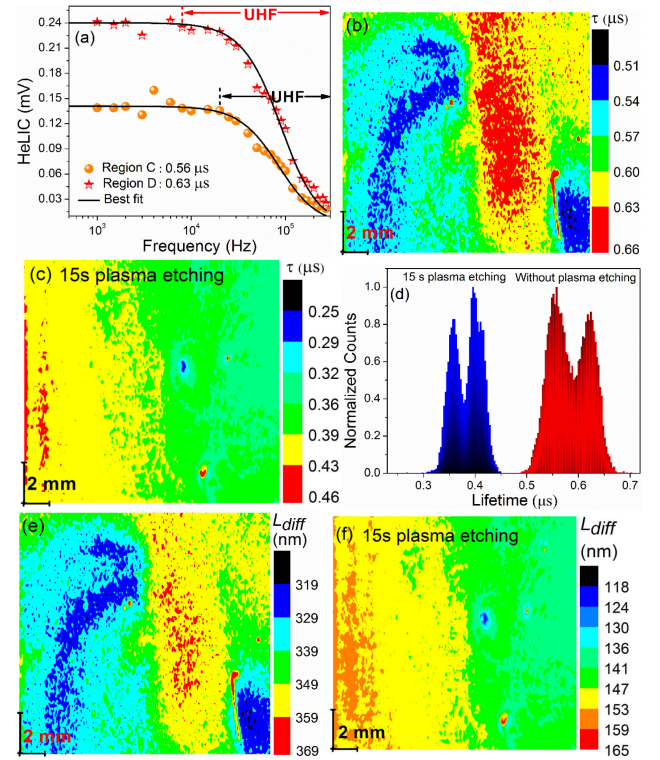

Fig. 4. (a) Frequency-dependent average-amplitude HeLIC image for regions C and D of the CQD solar cell shown in Fig. 3(a) without plasma etching, also showing the definition of the UHF range. (b) Lifetime image of the same CQD solar cell. (c) Lifetime image of a CQD solar cell of the same type after 15-s plasma etching. (d) Statistical lifetime distribution histogram for the above CQD solar cells with and without plasma etching. (e) and (f) exhibit the carrier diffusion length for CQD solar cells without and with plasma etching, respectively.

Fig. 3(a) and (b). The measured carrier lifetime values from HeLIC images, reconstructed from best-fitting individual pixel frequency profiles with no need for conventional calibration, are comparable with those measured with transient photovoltage for PbS CQD solar cells (3–6 μs) [23], impedance spectroscopy for PbS CQD thin films (3 μs) [24], time-resolved PL spectroscopy for PbS-capped CQDs (1 μs) and for CdSe nanocrystals (0.88 μs) [25], and with absorbance spectroscopy for PbS CQDs (1–1.8 μs) [26]. Additionally, for a PbS CQD type solar cell similar to ours, except for the PbS-PbX$_2$/AA [see Fig. 2(a)] replacement by PbS-tetrabutylammonium iodide surface passivation, Wang *et al.* [27] reported a carrier lifetime of ca. 0.5 μs using impedance spectroscopy. Compared with those carrier lifetime literature data, the slightly lower lifetime measured in this paper may be attributed to the diverse types of samples and/or to the quantitative imaging of a clearly inhomogeneous sample, as the previously measured parameters were the results of averaging over the entire solar cell. Furthermore, it should be noted that the CQD solar cells characterized in this study are not those with our highest efficiency that are expected to have even higher carrier lifetimes. It is important to recall that the carrier lifetimes characterized by various transient methodologies were traditionally obtained through fitting the time-dependent PL (or other electrical parameters, such as photovoltage) decay

spectrum to a simplified exponential decay model, which is also commonly used for lifetime extraction of thin films. It is apparent that the complexity of carrier transport behavior via various pathways in CQD solar cell devices has been ignored, possibly leading to deviations from the actual carrier lifetime in measurement. It is interesting to mention that the lifetime image in Fig. 4(b) resembles the UHF-HeLIC onset image in Fig. 3(a) and other $f_{\mathrm{UHF}} \geq 10$-kHz images. The dependence of HeLIC amplitude on modulation frequency can directly reflect carrier lifetime through a simplified model $f_k \sim 1/(2\pi\tau)$, in which f_k is the "knee" frequency at which the amplitude starts to drop, as shown in Fig. 4(a). It is re-emphasized that without the UHF-range modulation ability, HeLIC imaging would not be able to resolve lifetimes and other transport parameters, such as diffusion lengths of CQD solar cells and other PV and general optoelectronic devices. Examples of other transport parameter images are discussed ahead.

Oxygen plasma dry etching creates trap states in CQD solar cells, representing an additional way of investigating the influence of optoelectronic defect and trap states on carrier lifetimes and demonstrating the sensitivity of UFH-HeLIC imaging. Specifically, oxygen gas plasma is efficient in breaking chemical bonds and ligands of PbS CQDs, thereby creating extra chemical dangling bonds on the surface of quantum dots and ligand agents. Oxygen species, including ionized oxygen, can be added to CQDs to increase interstitial-associated oxygen defects. These effects on the CQD solar cell from oxygen plasma dry etching are expected to reduce carrier lifetime through enhanced non-radiative recombination induced by the increased material trap states and defects. The lifetime distribution image of an oxygen plasma etched CQD solar cell is shown in Fig. 4(c) and is plotted as a histogram in Fig. 4(d) along with the carrier lifetime distribution of the intact CQD solar cell. The two dominant lifetime peak distributions shown in Fig. 4(d) for both CQD solar cells with and without plasma etching may originate from the nature of the sample itself as regions with distinct image patterns, and were deliberately chosen for characterization. The difference in FWHM of the two lifetime distributions can be attributed to the homogenizing nature of the plasma-etched CQD solar cell or the plasma etching effects as manifested by the significant narrowing of the FWHM after plasma etching. Furthermore, as shown in Fig. 4(e) and (f), quantitative carrier diffusion length L_{diff} images of the above-mentioned solar cells without and with 15-s plasma etching were also constructed through $L_{\mathrm{diff}} = \sqrt{\tau D_e}$ where lifetime τ and diffusivity D_e were extracted using (5) and UHF-HeLIC imaging reconstruction from 27 frequency-dependent images. In this case, carrier-wave diffusion length exhibits image features similar to its lifetime constituent for both solar cells. As expected, an apparent L_{diff} decreases from ca. 340 nm that is consistent with the thickness of the CQD layer of our solar cell, to ca. 141 nm was observed due to enhanced defect or trap states induced from surface plasma etching.

To study the influence of surface recombination velocity on CQD solar cell performance, CQD/electrode interface effects were also investigated using UHF-HeLIC. Fig. 5(a) is a photograph of the CQD solar cell [structure shown in Fig. 2(a)]
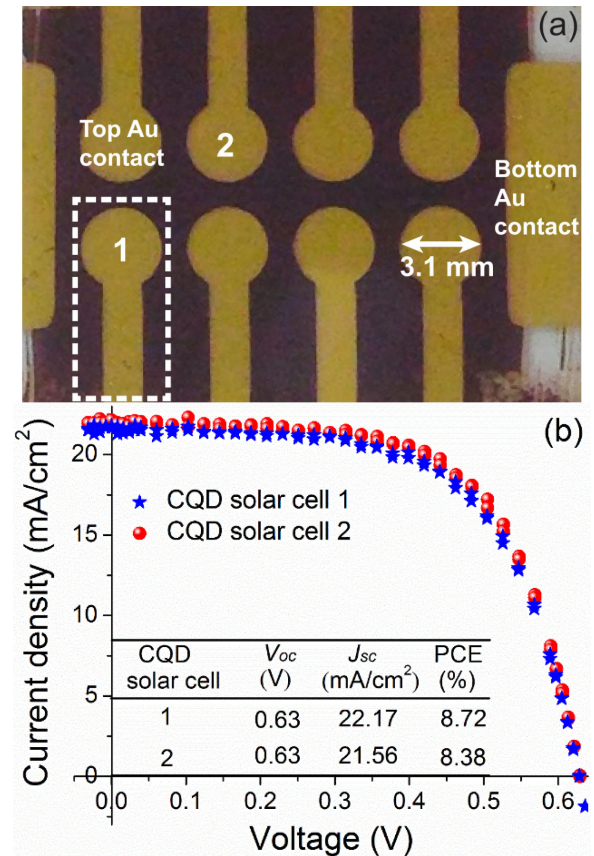

Fig. 5.   (a) Photograph of a typical CQD solar cell (without plasma etching) with Au contacts on top. Transparent glass was used as substrate for all CQD solar cells in this paper. (b) Current density versus voltage characteristics for the two selected CQD solar cell units 1 and 2, as shown in (a).

imaged with the Au contacts on top. The brown color regions are without Au contact deposition. Two high-efficiency CQD solar cell units 1 and 2 were selected and characterized with power conversion efficiencies (PCEs) as high as 8.72% and 8.38%, respectively, as shown in Fig. 5(b), whereas the efficiency of the highest PCE of our CQD solar cell was certified to be 11.28% [28]. To further investigate the interface influence and carrier transport parameters of solar cell unit 1, the HeLIC image of which is shown in Fig. 6(a) at 400 Hz and 200 K, quantitative parameter images were reconstructed and are shown in Fig. 6(b)–(e). The carrier transport diffusivity image was reconstructed using the same method as for carrier lifetime images in Fig. 4 through theoretical fitting of the experimental UHF-HeLIC images to (5). Furthermore, the diffusion length image in Fig. 6(d) was reconstructed in the same manner as in Fig. 4(e) and (f), whereas for the carrier drift length image, the equation $L_{\mathrm{diff}} = \sqrt{\tau \mu_e E}$ was used, where mobility μ_e was approximated using the Einstein relation. The net electrical field E was taken to be 1.2×10^4 V/cm according to the CQD solar cell thickness and the open-circuit voltage. For the complete solar cell with Au contact coating, τ was measured to be ca. 2.7 μs at 200 K with evidently slightly lower values within the Au/PbS-EDT regions. The reduced carrier lifetime can be attributed to enhanced trap states, acting as non-radiative recom-
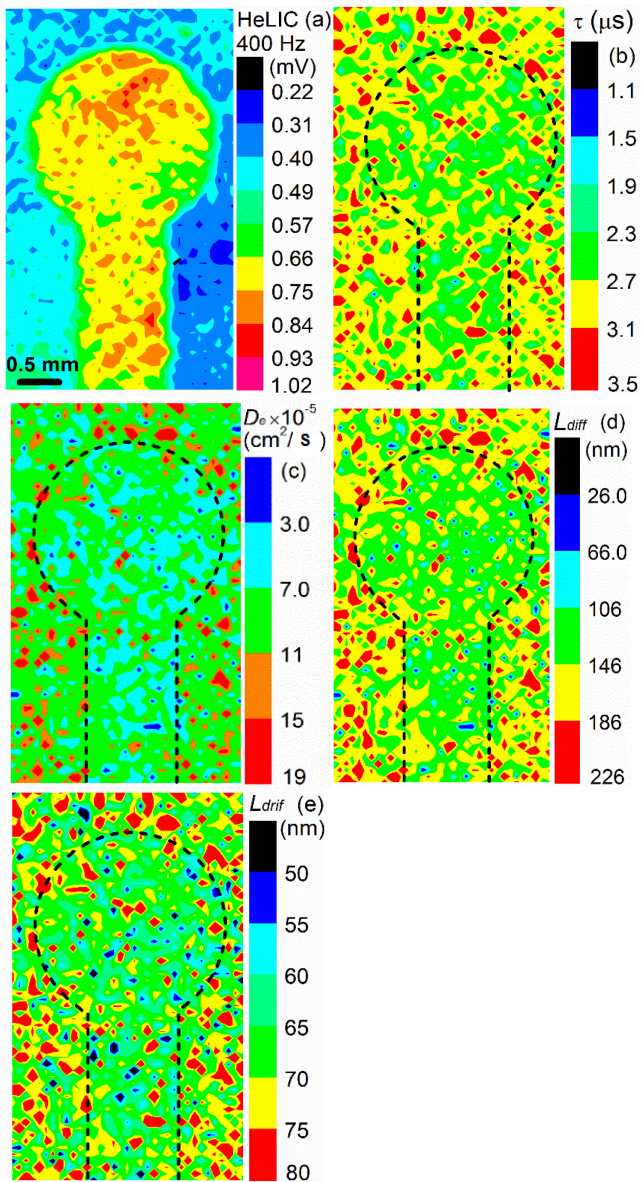
Fig. 6. (a) Quantitative HeLIC imaging of solar cell unit 1 at 400 Hz and 200 K. Applying CQD solar cell images at high frequencies, carrier transport parameters, (b) carrier lifetime τ, (c) diffusivity D_e, (d) diffusion length L_{diff}, and (e) drift length L_{drift} were reconstructed from series of HeLIC images in the UHF range.

bination centers and compromising carrier hopping lifetimes in the interface regions. Influenced by interface trap states, interface regions were found to exhibit lower diffusivity D_e (ca. 7×10^{-5} cm^2/s), diffusion length L_{diff} (ca.126 nm), and drift length L_{drift} (ca.65 nm) than the surrounding contact-free regions.

It should be noted that with the application of Au contacts onto our CQD solar cells, an aluminum thin plate with a smooth surface that can reflect light was placed under the cell to experimentally eliminate the potential Au-related reflection induced effects on the HoLIC and HeLIC images. Although different regions in the HoLIC and HeLIC images exhibit amplitude contrast, the carrier transport parameters are not determined or affected by the absolute PL emission amplitude values of

the solar cell. However, as further elaborated ahead, the "knee" frequency in Fig. 4(a) at which the HeLIC amplitudes start to decrease drastically, bears direct relationship to the carrier lifetime and other carrier transport parameters. The dynamic nature of the LIC technique where quantitative information is extracted from the frequency response of the signals rules out any effects of Au-related reflection fluctuations across the surface on carrier transport parameter image construction and measurements.

VI. CONCLUSION

In conclusion, a quantitative ultra-high-frequency, camera-based, imaging technique was introduced for large-area characterization of fast transport processes including hopping excitonic transport and their dissociated photocarrier wave transport in PV devices. We demonstrated large-area UHF-HeLIC images up to 270 kHz through heterodyne nonlinear carrier density diffusion-wave mixing and its application to CQD solar cell carrier-density-wave transport parameter imaging, including sub-μs lifetimes, optoelectronic diffusivity, and diffusion and drift lengths. Through these carrier transport images, CQD solar cell regions coated with Au electrodes indicate the presence of interface-state-associated carrier density deterioration with electrode deposition. This is a critical finding as these interfaces may be responsible for limiting the solar efficiency of CQD PV devices. Therefore, UHF-HeLIC imaging is shown to be a non-destructive diagnostic technique with strong potential for large-area fast optoelectronic dynamic process characterization, including quantitative probing and imaging of solar cell surface and sub-surface (including *p-n* junction) properties.

REFERENCES

[1] U. Amita *et al.*, "The effect of illumination on the formation of metal halide perovskite films," *Nature*, vol. 545, pp. 208–212, 2017.
[2] M. Barth, R. Schuster, A. Gruber, and F. Cichos, "Imaging single quantum dots in three-dimensional photonic crystals," *Phys. Rev. Lett.*, vol. 96, no. 24, 2006, Art. no. 243902.
[3] K. Yang *et al.*, "Multimodal imaging guided photothermal therapy using functionalized graphene nanosheets anchored with magnetic nanoparticles," *Adv. Mater.*, vol. 24, no. 14, pp. 1868–1872, 2012.
[4] W. Min *et al.*, "Imaging chromophores with undetectable fluorescence by stimulated emission microscopy," *Nature*, vol. 461, no. 7267, pp. 1105–1109, 2009.
[5] K. Ramspeck, S. Reißenweber, J. Schmidt, K. Bothe, and R. Brendel, "Dynamic carrier lifetime imaging of silicon wafers using an infrared-camera-based approach," *Appl. Phys. Lett.*, vol. 93, no. 10, 2008, Art. no. 102104.
[6] Z. Hameiri *et al.*, "Photoluminescence and electroluminescence imaging of perovskite solar cells," *Prog. Photovoltaics, Res. Appl.*, vol. 23, pp. 21697–1705, 2015.
[7] T. Trupke, R. A. Bardos, M. C. Schubert, and W. Warta, "Photoluminescence imaging of silicon wafers," *Appl. Phys. Lett.*, vol. 89, no. 4, 2006, Art. no. 044107.
[8] J. A. Giesecke, M. C. Schubert, B. Michl, F. Schindler, and W. Warta, "Minority carrier lifetime imaging of silicon wafers calibrated by quasi-steady-state photoluminescence," *Solar Energy Mater, Solar Cells*, vol. 95, no. 3, pp. 1011–1018, 2011.
[9] Z. Hameiri and P. Chaturvedi, "Spatially resolved electrical parameters of silicon wafers and solar cells by contactless photoluminescence imaging," *Appl. Phys. Lett.*, vol. 102, no. 7, 2013, Art. no. 073502.
[10] C. Shen, H. Kampwerth, and M. A. Green, "Photoluminescence based open circuit voltage and effective lifetime images re-interpretation for solar cells: The influence of horizontal balancing currents," *Solar Energy Mater, Solar Cells*, vol. 130, pp. 393–396, 2014.

[11] C. Shen *et al.*, "Spatially resolved photoluminescence imaging of essential silicon solar cell parameters and comparison with CELLO measurements," *Solar Energy Mater, Solar Cells*, vol. 109, pp. 77–81, 2013.

[12] T. Fuyuki, H. Kondo, T. Yamazaki, Y. Takahashi, and Y. Uraoka, "Photographic surveying of minority carrier diffusion length in polycrystalline silicon solar cells by electroluminescence," *Appl. Phys. Lett.*, vol. 86, no. 26, 2005, Art. no. 262108.

[13] Z. Hameiri *et al.*, "Photoluminescence and electroluminescence imaging of perovskite solar cells," *Prog. Photovoltaics: Res. Appl.*, vol. 23, no. 12, pp. 1697–1705, 2015.

[14] M. Kasemann *et al.*, "Luminescence imaging for the detection of shunts on silicon solar cells," *Prog. Photovoltaics, Res. Appl.*, vol. 16, no. 4, pp. 297–305, 2008.

[15] Q. Sun, A. Melnikov, and A. Mandelis, "Quantitative self-calibrating lock-in carrierographic lifetime imaging of silicon wafers," *Appl. Phys. Lett.*, vol. 101, no. 24, 2012, Art. no. 242107.

[16] K. Ramspeck *et al.*, "Recombination current and series resistance imaging of solar cells by combined luminescence and lock-in thermography," *Appl. Phys. Lett.*, vol. 90, no. 15, 2007, Art. no. 153502.

[17] J. Liu, A. Melnikov, and A. Mandelis, "Contactless measurement of electrical parameters and estimation of current-voltage characteristics of Si solar cells using the illumination intensity dependence of lock-in carrierography (photoluminescence) images," *J. Appl. Phys.*, vol. 114, no. 10, 2013, Art. no. 104509.

[18] *Basic Electronics*. Millington, TN, USA: United States Bureau Naval Personnel, 1973, p. 338.

[19] L. Hu *et al.*, "Quantitative analysis of trap-state-mediated exciton transport in perovskite-shelled PbS quantum dot thin films using photocarrier diffusion-wave nondestructive evaluation and imaging," *J. Phys. Chem. C*, vol. 120, no. 26, pp. 14416–14427, 2016.

[20] A. Mandelis, J. Batista, and D. Shaughnessy, "Infrared photocarrier radiometry of semiconductors: Physical principles, quantitative depth profilometry, and scanning imaging of deep subsurface electronic defects," *Phys. Rev. B*, vol. 67, no. 20, 2003, Art. no. 205208.

[21] Q. Sun, A. Melnikov, and A. Mandelis, "Camera-based high frequency heterodyne lock-in carrierographic (frequency-domain photoluminescence) imaging of crystalline silicon wafers," *Phys. Status Solidi (a)*, vol. 213, no. 2, pp. 405–411, 2016.

[22] L. Hu *et al.*, "Temperature-and ligand-dependent carrier transport dynamics in photovoltaic PbS colloidal quantum dot thin films using diffusion-wave methods," *Solar Energy Mater. Solar Cells*, vol. 164, pp. 135–145, 2017.

[23] A. K. Rath *et al.*, "Solution-processed inorganic bulk nano-heterojunctions and their application to solar cells," *Nature Photon.*, vol. 6, no. 8, pp. 529–534, 2012.

[24] A. K. Rath, T. Lasanta, M. Bernechea, S. L. Diedenhofen, and G. Konstantatos, "Determination of carrier lifetime and quantum dot films via impedance spectroscopy," *Appl. Phys. Lett.*, vol. 104, no. 6, 2014, Art. no. 063504.

[25] J. H. Warner, E. Thomsen, A. R. Watt, N. R. Heckenberg, and H. Rubinsztein-Dunlop, "Time-resolved photoluminescence spectroscopy of ligand-capped PbS nanocrystals," *Nanotechnology*, vol. 16, no. 2, pp. 175–179, 2004.

[26] I. Moreels *et al.*, "Size-dependent optical properties of colloidal PbS quantum dots," *ACS Nano*, vol. 3, no. 10, pp. 3023–3030, 2009.

[27] H. Wang *et al.*, "Charge carrier conduction mechanism in PbS quantum dot solar cells: Electrochemical impedance spectroscopy study," *ACS Appl. Mater. Interfaces*, vol. 8, no. 28, pp. 18526–18533, 2016.

[28] M. Liu *et al.*, "Hybrid organic-inorganic inks flatten the energy landscape in colloidal quantum dot solids," *Nature Mater.*, vol. 16, pp. 258–263, 2017.

Authors' photographs and biographies not available at the time of publication.